

# Continuous statistics of the Ly $\alpha$ forest at $0 < z < 1.6$ : the mean flux, flux distribution, and autocorrelation from HST FOS spectra.

David Kirkman<sup>1</sup>\* David Tytler<sup>1</sup>, Dan Lubin<sup>1</sup>, and Jane Charlton<sup>2</sup>

<sup>1</sup> Center for Astrophysics and Space Sciences, University of California San Diego, La Jolla, CA, 92093-0424

<sup>2</sup> 525 Davey Lab, Dept. of Astronomy and Astrophysics, Penn State, University Park, PA, 16802

11 October 2018

## ABSTRACT

We measure the amount of absorption in the Ly $\alpha$  forest at  $0 < z < 1.6$  in Hubble Space Telescope Faint Object Spectrograph spectra of 74 QSOs. Starting with a 334 QSO sample compiled by Bechtold *et al.* 2002, we selected 74 QSOs that have the highest signal to noise and complete coverage of rest frame wavelengths 1070–1170 Å. We measure the absorption from the flux in each pixel in units of the unabsorbed continuum level. We mask out regions of spectra that contain metal lines, or strong Ly $\alpha$  lines that are accompanied by other Lyman series line or metals at the same redshift, leaving Ly $\alpha$  absorption from the low density intergalactic medium. At  $0 < z < 1.6$  we find that 79% of the absorption is from the low density intergalactic medium, 12% from metals and 9% from the strong H I lines, nearly identical to the percentages (78, 15 and 7) that we measured independently at  $z = 2$  from spectra taken with the Kast spectrograph on the Lick 3-m. At  $z = 1$  the low density intergalactic medium absorbs  $0.037 \pm 0.004$  of the flux. The error includes some but not all of the uncertainty in the continuum level. The remaining part gives relative errors of approximately 0.21 when we report the mean absorption in eight independent redshift intervals, and 0.047 when we average over all redshifts. We find 1.46 times more absorption from the low density intergalactic medium than comes from Ly $\alpha$  lines that Bechtold *et al.* 2002 listed in the same spectra. The amount of absorption increases with  $z$  and can be fit by a power law in  $(1 + z)$  with index 1.01. This corresponds to no change in the number of lines, of fixed rest frame equivalent widths, per unit redshift, consistent with the Janknecht *et al.* 2006 results on the distribution of lines. When we include similar measurements from higher redshifts, we need more degrees of freedom to fit the amount of absorption at  $0 < z < 3.2$ . A power law with a break in slope, changing from index 1.5 at low  $z$  to 3.0 above  $z \sim 1.1$  is a better but only marginally acceptable fit. We also calculate two other continuous statistics, the flux probability distribution function and the flux autocorrelation function that is non-zero out to  $v \sim 500$  km s $^{-1}$  at  $0.5 < z < 1.5$ .

**Key words:** quasars: absorption lines – cosmology: observations – intergalactic medium.

## 1 INTRODUCTION

The Ly $\alpha$  forest seen in the spectra of distant QSOs is a key probe of the intergalactic medium (IGM) at redshifts  $z < 6$ . The Ly $\alpha$  forest is produced by neutral Hydrogen and so probes both the distribution of matter and the ionization state of the IGM. We have been working on extracting the properties of the IGM from detailed comparisons of Ly $\alpha$

forest observations with grids of numerical cosmological simulations (Tytler *et al.* 2004; Jena *et al.* 2005; Kirkman *et al.* 2005).

The simplest measurement to make of the Ly $\alpha$  forest is the average absorption. This is sometimes reported as a mean flux  $\overline{F}$  or as an effective opacity  $\tau_{\text{eff}}$ , but in this paper we follow the convention of Oke & Korycansky (1982) and report DA = 1 –  $\overline{F}$ , where DA stands for the flux Decrement in the Lyman Alpha region of a QSO spectrum. DA and its redshift evolution have long been known to place important constraints on the properties

\* E-mail: dkirkman@ucsd.edu

of the IGM (Jenkins & Ostriker 1991). Numerous authors have noted that measurements of DA can constrain key cosmological and astrophysical parameters such as the baryon density  $\Omega_b$ ,  $\sigma_8$ , the temperature density relationship of the IGM, and the intensity of the UV background  $\Gamma_{912}$  (Hernquist et al. 1996; Rauch et al. 1997; Rauch 1998; McDonald & Miralda-Escudé 2001; Tytler et al. 2004). Recent work at high redshift has focused on using the evolution of DA as a probe of the ionization state of the IGM (Songaila 2004; Bernardi et al. 2003). We (Tytler et al. 2004; Jena et al. 2005; Kirkman et al. 2005) used the combination of DA and the distribution of line widths to show which combinations of cosmological and astrophysical parameters give numerical simulations of the Ly $\alpha$  forest that best match spectra.

DA or the mean flux is an example of a continuous statistic that is defined at all wavelengths in a spectrum. A complementary set of discrete statistics are also widely used. These begin with a list of absorption lines in a spectrum, each of which has fitted properties, such as equivalent width  $W$ , and central wavelength. One such line counting statistic is the number of lines with  $W$  exceeding some minimum as a function of redshift.

Most prior work at low redshifts used line counting (Bahcall et al. 1993, 1996; Weymann et al. 1998; Jannuzzi et al. 1998; Dobrzycki et al. 2002; Janknecht et al. 2006). The decrease in the number of lines near to QSOs has been used to estimate the intensity of the ultraviolet background (UVB) (Kulkarni & Fall 1993; Shull et al. 1999; Scott et al. 2000, 2002). At the lowest redshifts, QSOs and Seyfert galaxies are bright enough to allow high resolution spectra that also give line widths and hence column densities (Shull et al. 1999; Penton et al. 2000a, 2000b, 2004).

A major early result from HST QSO spectra was that the number of lines seen at  $z < 1.7$  was significantly more than expected from an extrapolation of the trend measured at higher redshifts. Davé et al. (1999) showed that in the context of numerical IGM simulations the evolution of the line counts was driven by a combination of cosmological expansion (which tends to increase ionization) and the fading of the UV background (which decreases H I ionization). The number of lines counted as a function of redshift is often fit with a broken power law with a shallower slope below  $z \sim 1.7$ . This is approximately the redshift where the ionization changes caused by the fading UV background become comparable with the ionization changes caused by the general expansion. At lower redshifts the drop in the UVB tends to cancel the expansion, leading to decreased evolution at lower redshifts. In more detail, the redshift of the break in slope is poorly known, and can be much lower than  $z = 1.7$ . Recently Janknecht et al. (2006) claimed the break is at  $z \sim 0.7$ .

The flux probability distribution function (PDF) gives the probability that a pixel will have a given flux value on a scale from zero to one at the continuum flux. This was first measured in the Ly $\alpha$  forest by Jenkins & Ostriker (1991). More recently, the flux PDF at  $z > 2$  has been derived from Keck + HIRES spectra (McDonald et al. 2000; Becker et al. 2006) and from a sample of SDSS quasars spectra (Desjacques et al. 2004). Becker et al. (2006) found that a simple description of the Ly $\alpha$  forest using a log-normal density distribution (Bi 1993; Bi & Davidsen 1997)

accurately reproduced the Ly $\alpha$  forest flux PDF between  $1.7 < z < 5.8$ . But Desjacques et al. (2004) also found that the same log-normal model failed to describe a large sample of SDSS spectra over a similar redshift range, unless they assumed surprisingly large 20% errors in the continuum levels used for the SDSS spectra.

In this paper, we use Hubble Space Telescope (HST) Faint Object Spectrograph (FOS) spectra to measure DA, the flux PDF and the flux autocorrelation function, a continuous version of the two point correlation function that is often applied to samples of absorption lines. We also combine these DA measurements with our earlier measurements at higher redshifts up to  $z = 3.2$ .

## 2 HST QSO SPECTRA

We measure the properties of the Ly $\alpha$  forest at rest frame wavelengths 1070 – 1170 Å in the spectra of bright QSOs. At low redshifts we must use UV spectra of QSOs, nearly all of which are from HST, since IUE spectra are largely superseded by HST spectra of the same QSOs. We considered HST spectra from FOS, GHRS and STIS, and chose the FOS spectra for this project. The moderate resolution GHRS spectra with spectral resolution  $R=21,000$  are of little use because they have a small wavelength coverage. There are about a dozen QSOs with suitable high resolution STIS spectra (Milutinović et al. 2006; Janknecht et al. 2006) with  $R = 30,000$ . We will examine several of these to check our FOS results, but otherwise they are too few. We know from Tytler et al. (2004) that we need many tens of spectra to average over the huge variations in the amount of absorption from QSO to QSO, and only FOS has observed this many QSOs. We did not consider the low resolution STIS spectra.

We use the atlas of 334 HST FOS spectra published by Bechtold et al. (2002, B02), who collected all of the spectra of QSOs obtained with the FOS G130H, G190H, or G270H gratings and reduced with the STSDAS package. The spectra have a pixels of size 0.25 Å (G130H), 0.37 Å (G190H) and 0.52 Å (G270H), and 4 pixels per diode. These gratings together provide overlapping wavelength coverage from below 1200 to 3200 Å at a spectral resolution of approximately  $R=1300$  (FWHM 230 km s $^{-1}$ ) for the usual aperture width and guiding jitter.

For analysis, we selected spectra from the B02 archive that had an average signal-to-noise ratio  $\text{SNR} > 20$  per pixel between 1070 – 1170 Å, and complete coverage of the Ly $\alpha$  forest between the Ly $\alpha$  and the Ly $\beta$  emission lines of the QSO. These two criteria leave 71 QSOs that we list in Table 1. We deliberately added three more QSOs with lower SNR (3C298, Q1026-0045B, Q1258+285) to give more spectra at the highest redshifts and 74 in total. These are amongst the brightest QSOs in the sky at low redshifts, and we are not aware of any factors in their selection that would bias a DA measurement. We restrict the sample to QSOs with high SNR and complete coverage of the Ly $\alpha$  forest because we know that the continua that we fit have significantly higher errors otherwise.

Most of the QSOs listed in Table 1 have spectra from multiple FOS gratings. To combine the data sets from different gratings, we re-sampled the spectrum from each grating onto a common wavelength scale, and then combined

the separate data sets pixel by pixel. For the pixels in the overlap region between gratings, we took the SNR weighted mean of the two observations. The B02 spectra are well calibrated, and there are no apparent artifacts in the spectrum overlap region between adjacent gratings.

### 3 PREPARATION OF THE SPECTRA

We fit continua to the FOS spectra manually, using B-splines and the software described in Kirkman et al. (2005). Two of us independently (DK and DT) fit continua to each spectrum. We examined the fits using plots with various aspect ratios, wavelength scales, and ordering. We discussed the fits and the differences and then we independently made slight adjustments. We repeated this process four times until we agreed, either in the continuum level, or that there was more than one reasonable interpretation of a spectral feature. Typically this comes down to a decision on whether a given region contains a weak emission line, correlated photon noise, or a group of weak absorption lines. We found that both the discussions and iterations were essential.

We developed a procedure to make the continua levels consistent among the QSOs. We plot the whole spectrum and an enlargement of only the region of interest. We fit the continua to spectra displayed with a bin size of 1 Å for all HST gratings because this larger pixel reduces the clutter of having 4 pixels per resolution element, and helps us see the continuum level. We also plot the residuals from the continua in units of the error in each pixel, and we work in both observed and rest wavelengths. We check, for example, that the DA and the residuals from the continuum fit do not depend on rest wavelength. We return to our continuum fits and the likely errors in them in §4, 7.

Because we are primarily interested in H I absorption from the low density IGM, we identified regions of each spectrum suspected of having either metal or high column density H I absorption. We first flagged wavelengths at  $\pm 3$  Å of  $z = 0$  Galactic metal absorption in every spectrum, whether or not we could see such absorption in a particular spectrum. We then flagged all pixels within  $\pm 3$  Å of each metal line identified by B02. We analyze the spectra with different regions included or excluded. If we exclude a pixel from the sum used to measure a DA value, we call this a masked region.

We define strong H I lines as any that B02 had identified as H I. These are typically absorption systems with higher H I columns which show either metal lines in low resolution FOS spectra or Lyman series lines. Fewer than half of these strong H I lines will be in Lyman limit systems (LLS). This procedure will not remove a statistically complete sample of high column density H I lines. It is a compromise to make use of the limited information in the FOS spectra. We mask regions within  $\pm 3$  Å of each identified metal line and the strong H I lines. In some cases, such as for damped Ly $\alpha$  lines, we mask a wider region of the spectrum to cover the absorption feature. In Fig. 1 we show examples of spectra with continua and flagged regions.

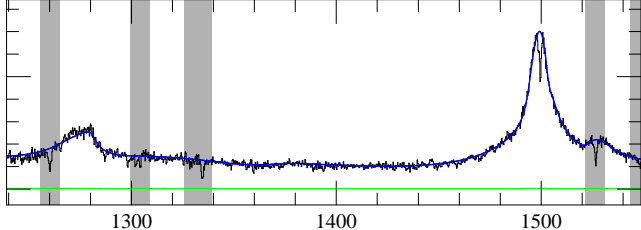
**Table 1.** The 74 QSOs with FOS spectra used to measure the Ly $\alpha$  forest absorption. QSOs for which we have also analyzed STIS spectra are indicated with a <sup>1</sup> after their name.  $z_{\text{forest}}$  is the mean redshift of the Ly $\alpha$  forest region analyzed.

Name	RA (J2000)	Dec (J2000)	$z_{\text{em}}$	$z_{\text{forest}}$	Ly $\alpha$ F SNR
MARK132	10:01:29.8	+54:54:39	1.750	1.534	25
PG1115+080A1	11:18:16.9	+07:45:59	1.722	1.508	24
Q1026-0045-B	10:28:37.0	-01:00:28	1.530	1.331	13
PKS0743-67	07:43:31.7	-67:26:25	1.511	1.313	22
PG0117+213 <sup>1</sup>	01:20:17.3	+21:33:46	1.493	1.297	39
PG1630+377	16:32:01.1	+37:37:49	1.478	1.283	37
HS-1216+5032A	12:18:41.1	+50:15:36	1.450	1.257	22
PKS0232-04	02:35:07.3	-04:02:06	1.450	1.257	34
3C298	14:19:08.2	+06:28:34	1.436	1.244	18
0957+561B	10:01:20.9	+55:53:49	1.414	1.224	29
1E0302-223	03:04:49.8	-22:11:52	1.400	1.211	28
QSO-1258+285	13:01:00.9	+28:19:44	1.355	1.170	16
0454+0356	04:56:47.2	+04:00:53	1.345	1.160	29
PG1634+706 <sup>1</sup>	16:34:29.1	+70:31:32	1.337	1.153	115
PG1522+101	15:24:24.5	+09:58:29	1.324	1.141	47
Q1435-0134	14:37:48.3	-01:47:11	1.310	1.128	44
PG1008+133	10:11:10.8	+13:04:11	1.287	1.107	31
PG1241+176 <sup>1</sup>	12:44:10.8	+17:21:03	1.273	1.094	30
4C06.41	10:41:17.2	+06:10:17	1.270	1.091	30
PKS-1327-206	13:30:07.7	-20:56:17	1.169	0.998	28
PG1718+481 <sup>1</sup>	17:19:38.3	+48:04:12	1.084	0.920	83
PKS1229-02	12:32:00.0	-02:24:05	1.045	0.884	22
PG1248+401 <sup>1</sup>	12:50:48.3	+39:51:40	1.030	0.870	30
TON153	13:19:56.3	+27:28:08	1.022	0.863	46
PKS2145+06	21:48:05.5	+06:57:38	0.990	0.833	28
1148+5454	11:51:20.4	+54:37:32	0.969	0.814	29
TON157	13:23:20.5	+29:10:07	0.960	0.806	25
Q0107-025A	01:10:13.1	-02:19:54	0.948	0.795	25
PG1407+265	14:09:23.9	+26:18:21	0.944	0.791	50
Q0107-025B	01:10:16.3	-02:18:53	0.942	0.789	29
PKS2340-03	23:42:56.6	-03:22:26	0.896	0.747	42
PKS1252+11	12:54:38.2	+11:41:06	0.871	0.724	23
3C454-3	22:53:57.8	+16:08:53	0.859	0.713	29
CSO176	12:52:25.0	+29:13:21	0.820	0.677	27
PKS1424-11	14:27:38.1	-12:03:49	0.806	0.664	26
3C110	04:17:16.7	-05:53:46	0.781	0.641	36
CSO179	12:53:17.5	+31:05:50	0.780	0.640	34
CT336	01:04:41.0	-26:57:08	0.780	0.640	24
0959+68W1	10:03:06.8	+68:13:17	0.773	0.633	26
PG1538+477	15:39:34.8	+47:35:30	0.770	0.631	37
OS562	16:38:13.5	+57:20:23	0.745	0.608	20
PKS1354+19	13:57:04.5	+19:19:06	0.719	0.584	23
PKS2352-34	23:55:25.6	-33:57:55	0.706	0.572	27
B20923+39	09:27:03.0	+39:02:20	0.699	0.565	29
PKS2344+09	23:46:36.9	+09:30:46	0.672	0.540	31
3C57	02:01:57.2	-11:32:34	0.669	0.538	52
PKS0637-75	06:35:46.7	-75:16:16	0.656	0.526	20
3C263	11:39:57.1	+65:47:49	0.652	0.522	32
MC1104+167	11:07:15.0	+16:28:02	0.634	0.505	37
PKS2243-123	22:46:18.2	-12:06:51	0.630	0.502	39
PKS0044+030	00:47:05.9	+03:19:55	0.624	0.496	21
3C95	03:51:28.6	-14:29:09	0.616	0.489	51
4C41.21	10:10:27.5	+41:32:39	0.611	0.484	36
PKS0405-12	04:07:48.4	-12:11:36	0.574	0.450	66
PKS0454-22	04:56:08.9	-21:59:09	0.534	0.413	37
PKS0003+15	00:05:59.2	+16:09:49	0.450	0.336	42
HS0624+6907	06:30:02.7	+69:05:03	0.374	0.266	61
PG1216+069	12:19:20.9	+06:38:39	0.334	0.229	42
TON28	10:04:02.6	+28:55:35	0.329	0.224	55
PKS2251+11	22:54:10.4	+11:36:38	0.323	0.219	30
3C249.1	11:04:13.9	+76:58:58	0.311	0.208	50

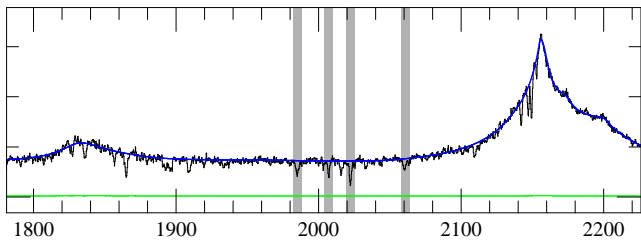
**Table 2.** Table 1 (continued)

Name	RA (J2000)	Dec (J2000)	$z_{\text{em}}$	$z_{\text{forest}}$	Ly $\alpha$ SNR
4C73.18	19:27:48.5	+73:58:01	0.302	0.200	36
B22201+31A	22:03:15.0	+31:45:37	0.297	0.195	75
E1821+643	18:21:57.2	+64:20:36	0.297	0.195	95
PG1444+407	14:46:45.9	+40:35:07	0.267	0.167	43
PG0953+414	09:56:52.4	+41:15:23	0.239	0.141	46
PG1427+480	14:29:43.1	+47:47:26	0.221	0.125	39
PG0947+396	09:50:48.4	+39:26:51	0.206	0.111	38
PG1322+659	13:23:49.5	+65:41:48	0.168	0.076	45
1402+2609	14:05:16.2	+25:55:33	0.164	0.072	52
PG1226+023	12:29:06.7	+02:03:08	0.158	0.067	291
PG1115+407	11:18:30.3	+40:25:55	0.154	0.063	40
0026+129	00:29:13.8	+13:16:03	0.142	0.052	59

PG0953+414



3C110



PG1630+377

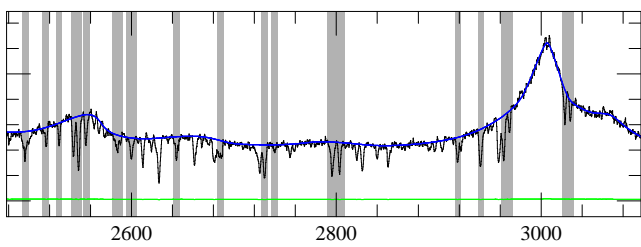


**Figure 1.** Examples of FOS spectra with continua. The wavelengths are observed frame Ångströms, and the vertical scale is linear flux with zero at the lowest long mark. The thin nearly flat line immediately above the zero level is the  $1\sigma$  error. These three QSOs have a range of redshifts and all have typical SNR. The shaded regions are pixels that we flag because they are within 3 Å of Galactic and other metal lines and strong H I lines. Some regions appear wider because there are several masked features near to each other (as in multi-component metal line systems).

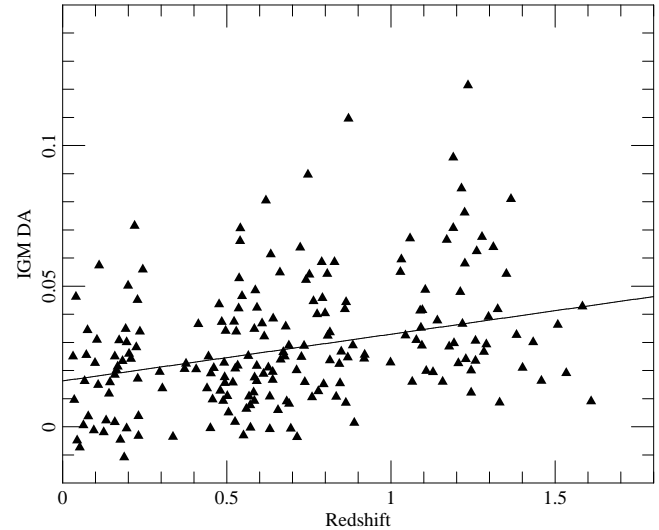


**Figure 2.** DA of the low density IGM vs. redshift. Metal lines and strong Ly $\alpha$  lines do not contribute because we masked those wavelengths. Each point shows the mean DA in 33.3 Å in the rest frame, with up to 3 points per QSO. The line is the best fit power law  $DA(z) = 0.016(1 + z)^{1.01}$ .

#### 4 DA IN THE FOS SPECTRA

We define  $DA = \langle 1 - f_i/c_i \rangle$  where  $f_i$  is the flux in pixel  $i$  and  $c_i$  is the continuum level in the same pixel. We restrict our analysis to the rest frame interval 1070 – 1170 Å, which we divide into three intervals 1070 – 1103 Å, 1103 – 1137 Å, and 1137 – 1170 Å. This gives 3 measurements of DA per QSO. This is a change from our choice at higher redshifts where we averaged the DA over intervals of redshift path 0.1, or 121.56 Å in the observed frame, or 121.56/(1 +  $z$ ) in the rest frame. At redshift  $z = 1.7$  these intervals are very similar to those we now use for HST spectra with fixed rest frame. We discard wavelength intervals with  $< 70\%$  of pixels remaining after the above masking procedure.

In Figure 2 we show the DA from the low density IGM alone as a function of redshift. The points shown do not include pixels masked because they are flagged as metals or strong H I lines. All 74 QSOs contribute to this figure, but for many QSOs one or occasionally two of the three wavelength regions are not used because they lacked sufficient non-flagged pixels. At  $z = 1$  each point on the plot includes pixels from a  $z$  range of 0.0548, hence all three points from each QSO appear in the same part of the plot. The relative lack of points at  $z=0.3$  and  $0.95$  is caused by the  $z$  distribution of the QSOs in the HST archive and the SNR in the Ly $\alpha$  forest of those spectra. The negative DA values show a combination of the true amount of absorption, the continuum level errors and photon noise. The large dispersion in the points at a given  $z$  is largely real variability in the IGM. The occasional very high points typically have two conspicuous deep lines that were not masked. The mean absorption apparently increases  $z$ .

We also show a power law  $DA(z) = A(1 + z)^\alpha$  which is a fit to these points, not to the DA per pixel. We found  $A = 0.016$  and  $\alpha = 1.01$ . We will not give errors on  $A$  and  $\alpha$  because the two parameters are strongly anti-correlated. For fixed  $A = 0.016$ ,  $\sigma_\alpha = 0.11$ , and for fixed  $\alpha = 1.01$ ,

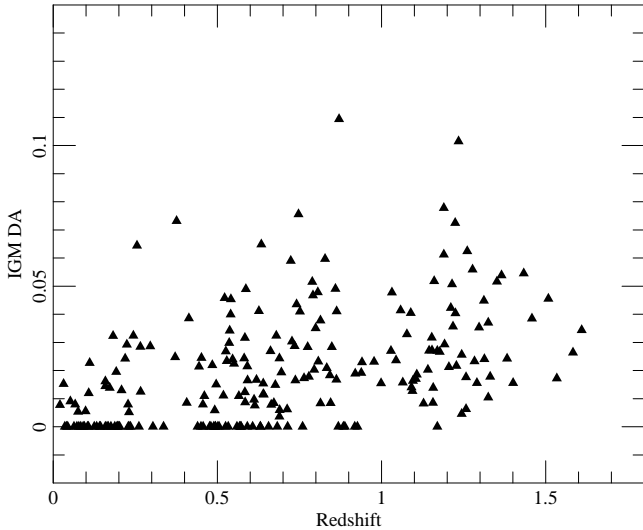


**Figure 3.** As Fig. 2 for the same QSOs and spectra but calculated by summing the equivalent widths of line listed in B02. This method gives less absorption than we measure from the flux in each pixel.

$\sigma_A = 0.001$ . However it is not unusual to see the value of  $\alpha$  change by many tenths for common changes in the sample of spectra.

In Table 3 we list values obtained from the points shown in Figure 2, binned into widths of  $\delta z = 0.2$ , where the first bin covers  $0.1 < z < 0.3$ . The column labeled “IGM” shows the total DA from the low density IGM alone, that is with the metals and strong H I lines masked. The column  $\sigma_{\text{IGM}}$  is the standard deviation of the points in the bin, divided by the square root of the number of points (the standard error). The column “All H” includes pixels flagged as H I lines, while the column labeled “Total” includes all pixels not flagged as Galactic absorption. The column labeled “Metal” uses only those pixels flagged as metal lines, column labeled “IDH” refers to the strong lines that were Identified as H by B02. The values given in the column “All H” are defined as the sum of IGM + IDH. The IDH values are approximately constant with  $z$ , with a mean of 0.0032. The metal absorption has a mean value of 0.0045 averaged over all redshifts in the FOS data, and it systematically increases with increasing redshift.

When we ignore redshift and take the mean for the whole sample, we find the total absorption of  $DA = 0.0371$  is comprised of 0.0293 (79%) low density IGM, 0.0043 (12%) metals, and 0.0034 (9%) strong H I lines. The signal is dominated by the low density IGM, just as we found at  $z = 2$  where the values were 78, 15 and 7% (Tytler et al. 2004).

The  $\sigma_{\text{IGM}}$  is a representation of the error on the DA that we list for the IGM alone. The external error is probably larger, because the points are not fully independent; there are large scale correlations in the amount of absorption across spectra, and systematic errors such as continuum level placement also extend across spectra.

The external error is also larger because the continuum level errors are partly but not completely contained in the errors that we quote in Table 3. The relative difference in IGM DA for our two continuum fits (that is, the difference in our DA values at each redshift divided by the mean DA at

that redshift) has a root mean squared value of 0.21. This is about the same size as the  $\sigma_{\text{IGM}}$  that we list in Table 3, which we take to mean that our errors due to continuum fitting and the (Poisson like) uncertainty due to our sampling of large scale structure are similar in magnitude. Immediately prior to finalizing our continuum fits, we had two relatively independent fits, that gave mean DA values averaged over all  $z$ , and these two DA values differed by a factor of 1.049. Earlier in the fitting process, the two continua differed by much larger amounts, for reasons that were apparent and which were taken into account as we iterated on the continuum fitting. The values given here are far from a precise measurements of the external errors, but they may indicate the approximate size of the error from continuum fitting alone. We speculate that the external errors for the IGM DA are of order 1.4 to 2 times the values given in Table 3 for redshift intervals of 0.2.

The effect of a given change in the continuum level on the DA value depends on the distribution of the absorption line depths. The lower the spectral resolution, the shallower the lines, and the more sensitive the DA to a given continuum level change. If the evolution of the DA with  $z$  is primarily a change in the number of lines and not in the line depths, then a given change in continuum level will produce the same relative change in DA at all  $z$ . We know, for example, that strong (typically deep) lines are increasingly common at higher  $z$  (Janknecht et al. 2006), which will make DA less sensitive to a given fractional error in the continuum.

The five QSOs indicated in Table 1 have STIS as well as FOS spectra. In Figure 4 we compare the DA measured from both spectra, in our three wavelength bins. This shows that our continuum placements and masks yield similar DA values, irrespective of the instrument. The masks for the STIS spectra are from Milutinović et al. (2006) while those for the FOS spectra are from B02. In Figure 5 we show the two spectra for PG 0117 which has intermediate SNR STIS and FOS spectra. We would expect the continua on the STIS spectra to be more accurate, since more photons are recorded per spectrum, while Milutinović et al. (2006) have made a concerted effort to make the metal line identifications complete.

We also calculate a version of DA for the low density IGM by summing the W values that B02 give for the unidentified lines in the spectra of the 74 QSOs. We measure this DA in the same redshift bins that we used in Fig. 2. In each bin we obtain DA by subtracting the observed frame W values from the observed frame path length in Ångstroms, and dividing the result by the path length. The results in Fig. 3 show general similarity with the DA defined from the flux in Fig. 2 except that the flux DA shows more absorption, as we might expect. When we use the flux in pixels to measure DA, we can detect absorption from features that do not make the threshold to count as reliable lines. For these FOS spectra, the line threshold varies from spectrum to spectrum, following the SNR. When we average over all  $z$ , the two DA values for the low density IGM are 0.020 from the lines, and 0.029 from the flux, larger by a factor of 1.46.

Following Weymann et al. (1998), Dobrzycki et al. (2002) fit the number of lines in the 336 B02 spectra with a power law in redshift and an exponential in rest equivalent width

**Table 3.** DA as a function of redshift from rest frame wavelengths 1070 – 1170 Å in FOS spectra of the 74 QSOs

$z$	IGM	$\sigma_{\text{IGM}}$	All H	$\sigma_{\text{AllH}}$	Total	$\sigma_{\text{Total}}$	Metal	$\sigma_{\text{Metal}}$	IDH	$\sigma_{\text{IDH}}$
0.20	0.020	0.003	0.023	0.003	0.024	0.003	0.000	0.000	0.003	0.003
0.40	0.020	0.003	0.022	0.003	0.024	0.003	0.002	0.002	0.003	0.002
0.60	0.026	0.003	0.028	0.003	0.031	0.003	0.003	0.001	0.003	0.001
0.80	0.035	0.004	0.042	0.005	0.045	0.005	0.003	0.001	0.007	0.002
1.00	0.037	0.004	0.040	0.004	0.049	0.006	0.010	0.004	0.003	0.002
1.20	0.045	0.005	0.047	0.005	0.057	0.005	0.010	0.003	0.002	0.002
1.40	0.039	0.007	0.043	0.010	0.051	0.013	0.008	0.004	0.004	0.004
1.60	0.027	0.007	0.027	0.007	0.044	0.012	0.017	0.007	0.000	-0.000

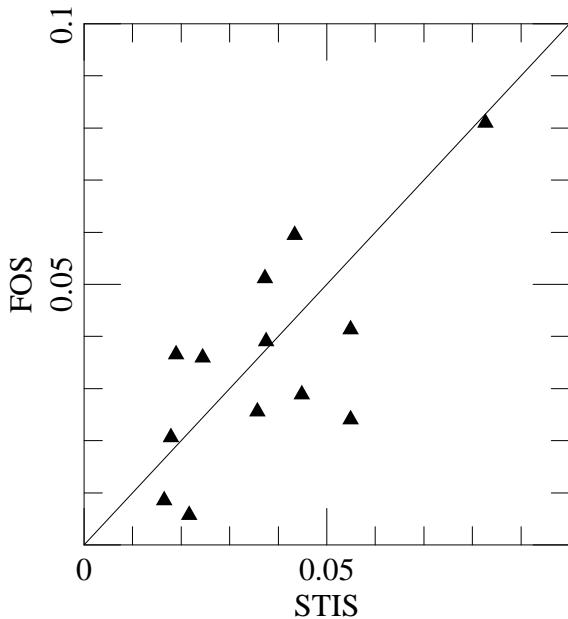


**Figure 4.** The DA from FOS spectra versus the DA from STIS spectra of the same objects. Five QSOs each contribute up to three points, each point using the flux from 33.3 Å in the rest frame. Three segments are not shown because more than 30% of their pixels were masked. The solid diagonal line shows expectation for ideal data and measurements.

$$\frac{\partial^2 N}{\partial z \partial W_{\lambda 0}} = A_0 W_*^{-1} (1+z)^\gamma e^{-W_{\lambda 0}/W_*}, \quad (1)$$

where  $W_{\lambda 0}$  is the rest equivalent width of a line, and  $A_0$ ,  $W_*$ , and  $\gamma$  are constants that are fit to match the observed distribution of line  $W_{\lambda 0}$ . The mean of the exponential distribution  $e^{-(W_{\lambda 0}/W_*)}$  from zero to infinity is  $W_*$ , so the mean of  $W_*^{-1} e^{-(W_{\lambda 0}/W_*)}$  is unity, and the number density of lines as a function of redshift is

$$\frac{\partial N}{\partial z} = A_0 (1+z)^\gamma. \quad (2)$$

Since the average observed equivalent width of a line at redshift  $z$  is  $W = W_*(1+z)$ , we find that the mean observed frame equivalent width of absorption as a function of redshift is, as usual, given by

$$\frac{\partial W}{\partial z} = W_* (1+z) \frac{\partial N}{\partial z} = A_0 W_* (1+z)^{\gamma+1}. \quad (3)$$

To convert to  $\text{DA}(z)$ , all we need to do is divide by the available observed frame path length per unit redshift,  $\partial \lambda / \partial z = \lambda_0$  where  $\lambda_0$  is the rest frame wavelength of the absorption line, or 1215.67 Å for H I Ly $\alpha$ . This gives

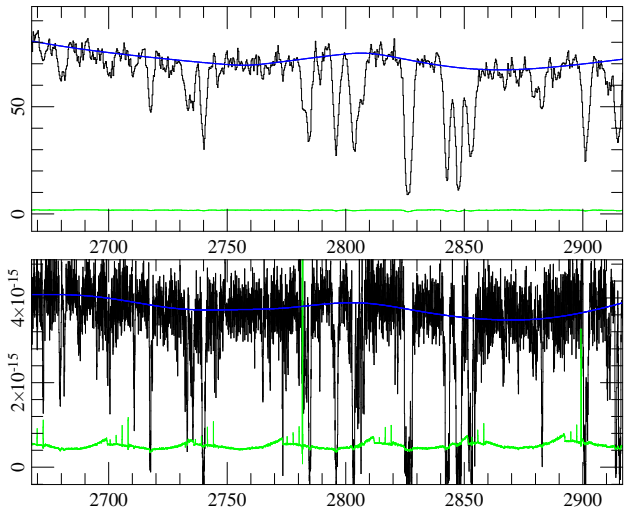


**Figure 5.** Rest frame wavelengths 1070 – 1170 Å in the FOS (top) and STIS (bottom) spectra of QSO PG 0117+213 at  $z_{\text{em}} = 1.493$ . The upper smooth curve is the continuum while the lower line just above zero is the  $1\sigma$  error. Known emission lines that vary in strength from QSO to QSO cause the continuum level to rise at either end and near the middle.

$$\text{DA}(z) = \frac{A_0 W_*}{\lambda_0} (1+z)^{\gamma+1}. \quad (4)$$

This shows that if the rest frame equivalent width distribution is independent of redshift and the number of lines per unit  $z$  changes as  $(1+z)^\gamma$ , then  $\text{DA}(z) \propto (1+z)^{\gamma+1}$ , where the extra one in the power comes from the increase in the observed equivalent width with  $1+z$ .

The exponent  $\alpha = 1 + \gamma = 1.01$  that we measured for the flux in the pixels in the FOS spectra is consistent with  $\gamma = 0$  which means no change in the number lines per unit redshift, if the lines have fixed rest frame equivalent widths. From Table 2 in Dobrzycki et al. (2002) we see that the evolution of Ly $\alpha$  forest lines in the FOS data is characterized by  $1 + \gamma \sim 1.5$ , larger than the value that we measured. Before we comment on this difference, we should look at the amplitudes.

For the “forest” sample with an equivalent width threshold of 0.24 Å, and no maximum  $W$  cutoff (line 6 of Table 2 in Dobrzycki et al. (2002)), the amplitude is  $A_0 W_*/\lambda_0 = 0.0048$ , about one third of what we find. But the line density  $A_0$  in Dobrzycki et al. (2002) is defined to give the density of lines with  $W > 0.24$  Å. To compare with DA we can alternatively extrapolate to

$W = 0$ , which increases their amplitude by a factor of  $\int_0^\infty e^{-W\lambda_0/W_*} / \int_{0.24}^\infty e^{-W\lambda_0/W_*} = 2.9$  when  $W_* = 0.22$  Å. This extrapolation gives an amplitude of 0.0139, similar to the 0.014 that we found from the flux in pixels. This agreement is slightly misleading because they include and we exclude strong H I lines.

It is possible to have both  $1 + \gamma = 1.0$  for the DA from flux in pixels, and  $1 + \gamma = 1.5$  for the lines with  $W > 0.24$  Å, since the latter includes only 1/3 of the absorption in the former. This would require that the stronger lines, the only ones seen in line counting, decline rapidly in number with decreasing redshift. The weaker lines that dominate the total absorption that we measure using the flux in the pixels change little. The more rapid evolution of the stronger lines has been reported before. Janknecht et al. (2006) found that lines with  $\log N_{\text{HI}} > 13.64$  cm $^{-2}$  had  $1 + \gamma = 2.50 \pm 0.45$  while lines with  $12.9 < \log N_{\text{HI}} < 14.0$  cm $^{-2}$  had  $1 + \gamma = 0.74 \pm 0.31$ , both for  $0.7 < z < 1.9$ . Janknecht et al. (2006) also note that the evolution is near zero at lower redshifts for even stronger lines. They find  $1 + \gamma = 1.13 \pm 0.06$  for the number of lines with  $W > 0.24$  Å at  $0 < z < 1.5$  from Weymann et al. (1998).

## 5 FOS FLUX PDF AND AUTOCORRELATION

We also calculate the probability distribution of the flux – the flux PDF – and the autocorrelation of the flux, two of the more common higher order continuous statistics. We use exactly the same spectra and masking to leave only the low density IGM that we used for the DA calculation. The center of mass of the PDF should be the DA value. This is unfortunately the only information that we can readily obtain from the PDF without knowing the spectral resolution and SNR for each pixel.

In Figure 6 and Table 4 we show the PDF in six panels, divided at redshifts 0.5 and 1.0 and showing the high SNR spectra alone.  $P(F)$  is normalized so that its integral over all  $F$  is unity. Some pixels have flux  $F$  above 1.0 because of a combination of photon noise and continuum level errors. We believe that our continuum level errors are smaller in units of  $F$  when the SNR is higher. The lower three panels use only pixels with  $\text{SNR} > 40$ . They show slightly fewer pixels with  $F > 1.0$ .

We see that the most likely  $F$  is in the range 0.975 – 1.025. This is expected if most pixels in the FOS spectra have  $DA < 0.025$ . If most pixels have  $DA < 0.025$  then the mean error in our continuum level is  $< 0.025$ . Alternatively if most pixels have  $DA > 0.025$  then the continuum error is large and unknown. At these low redshifts visible absorption lines occupy a relatively small part of each spectrum. If most of the total DA is in lines and not in a smooth GP absorption then we expect most pixels to be near the continuum.

The second most common flux value is that immediately below  $F=1.0$ , as we expect for absorption lines. The flux PDF in the lowest redshift bin is similar to a Gaussian, centered just below  $F=1.0$ , while at higher  $z$  we see a tail of lower  $F$  values from deeper lines. We do not see many pixels with  $F$  near zero. This is mostly because of the low spectral resolution, and also because we mask the strongest lines. If we use high resolution spectra that resolve all lines, most with column densities  $14 < \log N_{\text{HI}} < 17$  cm $^{-2}$  would reach

near zero flux, and some would not be masked using the criteria adopted here. Using only the higher SNR pixels gives somewhat narrower distributions, as we would expect, but this is a small change because all the spectra have relatively high SNR.

We calculated the autocorrelation of the flux in the 74 spectra in the interval 1070 – 1170 Å with the usual masks to leave only the low density IGM. We use a common definition for the autocorrelation at velocity lag  $v$

$$\xi(v) = \langle (F_i - \bar{F})(F_{i+v} - \bar{F}) \rangle \quad (5)$$

where  $F_{i+v}$  is the flux in a pixel separated from pixel  $i$  by a velocity  $v$  and  $\bar{F}$  is the mean flux in each spectrum, which differs from spectrum to spectrum. To estimate the uncertainty in  $\xi(v)$ , we divided each redshift interval into 16 separate samples, and took the standard deviation of the sub-samples.

In Figure 7 and Table 5 we show the results. The autocorrelation is non-zero to  $> 500$  km s $^{-1}$  ( $\sim 1\sigma$ ) for all three redshift intervals, and exceeds  $2\sigma$  out to  $\sim 400$  km s $^{-1}$  in lowest redshift bin and to  $\sim 500$  km s $^{-1}$  in the other two bins. Overall the autocorrelation is larger at higher redshifts. The velocity width of the signal is comparable to, but wider than expected from the spectral resolution. We see only marginal correlation beyond the spectral resolution and this is consistent with results at higher redshifts where high resolution spectra show little correlation beyond 150 km s $^{-1}$ . The points in each plot are highly correlated by construction, and hence it is unclear how much significance we should assign to the apparent broader distribution at higher redshifts. Janknecht et al. (2006) saw  $2\sigma$  correlation out to  $< 200$  km s $^{-1}$  for lower column density lines and to  $< 100$  km s $^{-1}$  for higher column density lines. The FOS spectra that we use here have more correlation at intermediate lags  $\sim 100$  km s $^{-1}$ , the  $\sigma$  of the Gaussian representing the line spread function. On larger scales the spectral resolution has limited effect, and the FOS spectra remain more sensitive because they contain 74 QSO spectra compared to the 9 STIS spectra used by Janknecht et al. (2006).

## 6 IGM H I OPACITY FROM $0 < Z < 3.2$

In Figure 8 we show the DA over a range of redshifts from the FOS data discussed here, from our Kast spectra (Tytler et al. 2004) and from our HIRES spectra (Kirkman et al. 2005). An extrapolation of the best fitting power law from  $1.6 < z < 3.2$  gives more absorption than we see at  $z \sim 1.5$ , but then less at the lowest redshifts. The power law fit to  $z < 1.6$  alone crosses that from higher  $z$  at  $z = 0.7$ .

In Table 6 we bin the DA values shown Fig. 8 in redshift intervals of 0.2. We list the mean DA in each bin and its error. The best fit single power law to the DA values in Table 6 from FOS, Kast and HIRES gives  $A = 0.0066$  and  $\alpha = 2.661$ , but with an unacceptably large  $\chi^2 = 41.1$  for 14 degrees of freedom. The fit improves significantly when we use a broken power law:

$$\text{DA}(z) = \begin{cases} A(1+z)^{\alpha_l} & : z < z_c \\ B(1+z)^{\alpha_h} & : z \geq z_c \end{cases} \quad (6)$$

where  $B = A(1+z_c)^{\alpha_l} / (1+z_c)^{\alpha_h}$ , and  $A$ ,  $z_c$ ,  $\alpha_l$ , and  $\alpha_h$

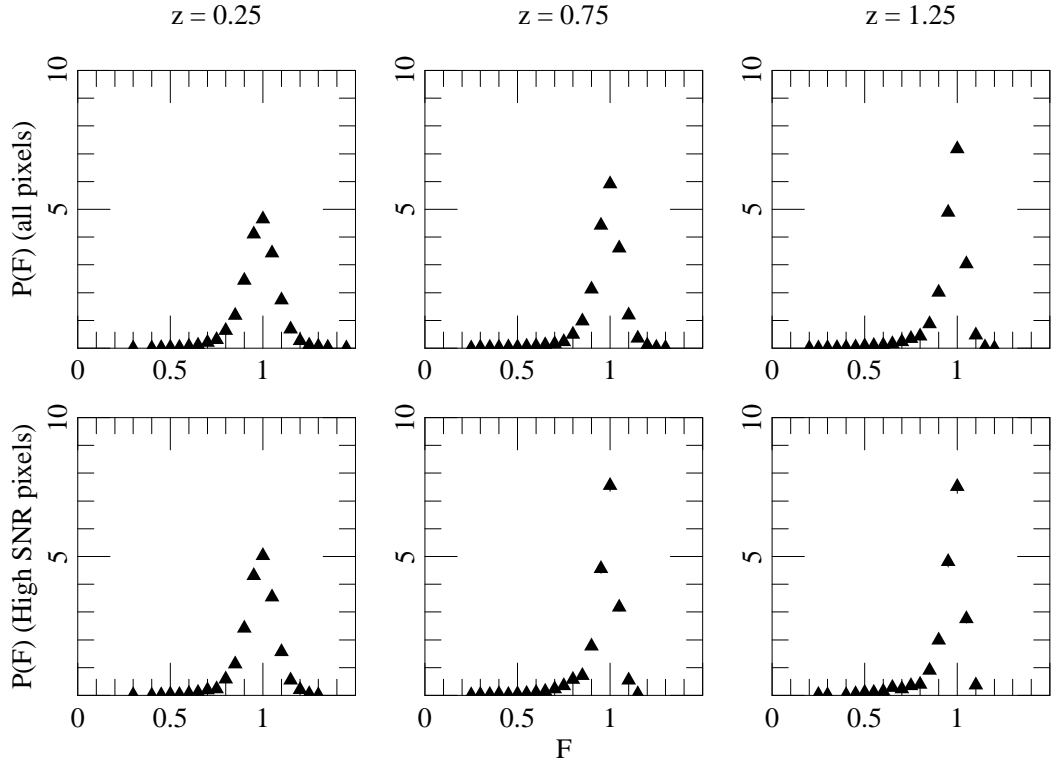


**Figure 6.** PDF of the flux in FOS spectra of the 74 QSO, from rest frame wavelengths  $1070 - 1170 \text{ \AA}$ . The PDF is evaluated in three independent redshift bins. There are 4 pixels per FOS diode. We masked pixels containing metal or strong Ly $\alpha$  lines, and hence these plots should contain absorption from only the low density IGM. The lower panels use the pixels with  $\text{SNR} > 40$  and the higher panels use pixels with all SNR values.

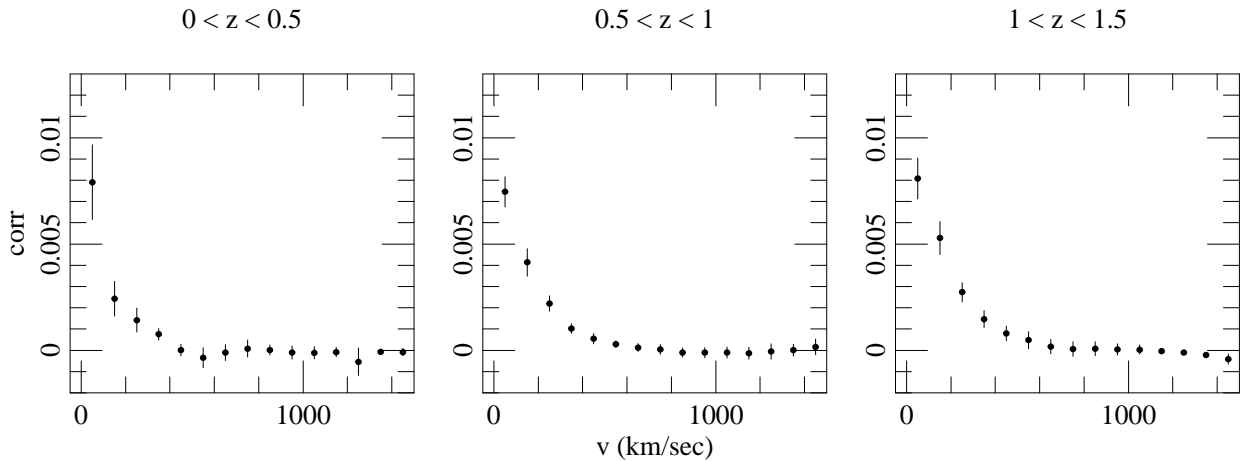


**Figure 7.** As Fig. 6 but showing the autocorrelation of the flux defined in Eqn. 5 as a function of velocity lag.

are free parameters. The best fit we can find ( $\chi^2 = 22.1$  for 12 degrees of freedom,  $\text{Prob}(\chi^2 > 22.1) = 4\%$ ), is not an excellent representation of the data. This fit has  $A = 0.013$ ,  $z_c = 1.1$ ,  $\alpha_l = 1.54$ , and  $\alpha_h = 2.98$ . Janknecht et al. (2006) found that the distribution of lines at  $0.5 < z < 1.9$  were fit with  $\alpha = 1.74 \pm 0.31$  from STIS spectra of nine QSOs, consistent with our  $\alpha_l$  value.

In Figure 9 we show the points from Table 6 and the broken power law. Although the data seem to depart from a simple smooth distribution at several redshift, this is probably an indication that we have underestimated the errors.

The data are noticeably lower than the fit at  $z = 1.4$ , for no known reason. This is the highest redshift bin that uses FOS spectra alone, and it samples redshifts where we have few spectra.

## 7 DISCUSSION AND CONCLUSION

We have presented common continuous statistics on the H I absorption in the low density IGM at  $0 < z < 1.6$ . We work mostly with the flux in each pixel, but also with line lists and fits to the distributions of lines.

**Table 4.** PDF of the flux at 1070 – 1170 Å in the FOS spectra of the 74 QSO, for the low density IGM pixels only. We have masked all the strong Ly $\alpha$  and metal lines.

F	0 < z < 0.5				0.5 < z < 1				1 < z < 1.5			
	All		High SNR		All		High SNR		All		High SNR	
	P(F)	$\sigma_{P(F)}$	P(F)	$\sigma_{P(F)}$	P(F)	$\sigma_{P(F)}$	P(F)	$\sigma_{P(F)}$	P(F)	$\sigma_{P(F)}$	P(F)	$\sigma_{P(F)}$
0.050	0.00	0.00	0.00	0.00	0.00	0.00	0.00	0.00	0.00	0.00	0.00	0.00
0.100	0.00	0.00	0.00	0.00	0.00	0.00	0.00	0.00	0.00	0.00	0.00	0.00
0.150	0.00	0.00	0.00	0.00	0.00	0.00	0.00	0.00	0.00	0.00	0.00	0.00
0.200	0.00	0.00	0.00	0.00	0.00	0.00	0.00	0.00	0.00	0.00	0.00	0.00
0.250	0.00	0.00	0.00	0.00	0.00	0.01	0.01	0.01	0.01	0.00	0.02	0.01
0.300	0.01	0.00	0.01	0.01	0.02	0.00	0.03	0.01	0.01	0.00	0.02	0.01
0.350	0.00	0.00	0.00	0.00	0.02	0.00	0.02	0.01	0.01	0.00	0.00	0.00
0.400	0.00	0.00	0.01	0.00	0.03	0.01	0.06	0.02	0.03	0.01	0.02	0.01
0.450	0.01	0.00	0.01	0.01	0.04	0.01	0.03	0.01	0.04	0.01	0.05	0.02
0.500	0.02	0.01	0.03	0.01	0.04	0.01	0.05	0.02	0.08	0.01	0.11	0.03
0.550	0.03	0.01	0.02	0.01	0.06	0.01	0.07	0.02	0.09	0.01	0.10	0.03
0.600	0.06	0.01	0.06	0.01	0.08	0.01	0.11	0.02	0.10	0.01	0.15	0.03
0.650	0.10	0.01	0.10	0.02	0.11	0.01	0.14	0.03	0.16	0.01	0.28	0.05
0.700	0.20	0.02	0.19	0.02	0.15	0.01	0.23	0.04	0.23	0.02	0.22	0.04
0.750	0.30	0.02	0.22	0.03	0.23	0.02	0.34	0.04	0.34	0.02	0.34	0.05
0.800	0.63	0.03	0.58	0.04	0.49	0.02	0.57	0.06	0.43	0.02	0.39	0.05
0.850	1.17	0.05	1.12	0.06	0.97	0.03	0.71	0.06	0.87	0.03	0.89	0.08
0.900	2.44	0.07	2.41	0.08	2.13	0.05	1.77	0.10	2.01	0.05	1.98	0.12
0.950	4.10	0.09	4.31	0.11	4.42	0.07	4.56	0.16	4.88	0.08	4.81	0.19
1.000	4.65	0.09	5.02	0.12	5.91	0.08	7.55	0.21	7.17	0.10	7.51	0.24
1.050	3.42	0.08	3.53	0.10	3.60	0.06	3.17	0.13	3.03	0.06	2.75	0.14
1.100	1.73	0.06	1.57	0.07	1.19	0.03	0.54	0.06	0.47	0.03	0.37	0.05
1.150	0.68	0.04	0.55	0.04	0.35	0.02	0.05	0.02	0.04	0.01	0.00	0.00
1.200	0.27	0.02	0.20	0.02	0.10	0.01	0.00	0.00	0.00	0.00	0.00	0.00
1.250	0.11	0.01	0.06	0.01	0.03	0.01	0.00	0.00	0.00	0.00	0.00	0.00
1.300	0.06	0.01	0.01	0.01	0.00	0.00	0.00	0.00	0.00	0.00	0.00	0.00
1.350	0.02	0.01	0.00	0.00	0.00	0.00	0.00	0.00	0.00	0.00	0.00	0.00
1.400	0.00	0.00	0.00	0.00	0.00	0.00	0.00	0.00	0.00	0.00	0.00	0.00
1.450	0.00	0.00	0.00	0.00	0.00	0.00	0.00	0.00	0.00	0.00	0.00	0.00
1.500	0.00	0.00	0.00	0.00	0.00	0.00	0.00	0.00	0.00	0.00	0.00	0.00

**Table 5.** As Table 4, but for the flux autocorrelation defined in Eqn. 5 as a function of the velocity in the center of the 100 km s<sup>-1</sup> wide bins.

v (km/sec)	0 < z < 0.5		0.5 < z < 1		1 < z < 1.5	
	$\xi$	$\sigma_{\xi}$	$\xi$	$\sigma_{\xi}$	$\xi$	$\sigma_{\xi}$
50.0	0.007906	0.001374	0.007456	0.000771	0.008080	0.001014
150.0	0.002431	0.000626	0.004138	0.000653	0.005285	0.000791
250.0	0.001419	0.000504	0.002193	0.000354	0.002733	0.000510
350.0	0.000760	0.000316	0.001022	0.000256	0.001471	0.000439
450.0	0.000009	0.000539	0.000544	0.000209	0.000788	0.000304
550.0	-0.000346	0.000426	0.000287	0.000149	0.000480	0.000425
650.0	-0.000104	0.000384	0.000126	0.000207	0.000173	0.000327
750.0	0.000082	0.000335	0.000044	0.000196	0.000062	0.000314
850.0	0.000012	0.000316	-0.000104	0.000205	0.000081	0.000279
950.0	-0.000103	0.000300	-0.000106	0.000205	0.000040	0.000268

DA(z) is a function that we have previously used at higher redshifts to deduce the physical properties of the IGM (Tytler et al. 2004). We generally require that simulations of the IGM should match the observed DA when they are using a concordant set of cosmological and astrophysical parameters. When these other parameters are known from other work, we can use DA to give the most accurate measurements of the intensity of the UV background radiation that ionizes the IGM.

The DA is an explicit and easy to understand mea-

surement of the total absorption by Ly $\alpha$  in the IGM. It is relatively easy to visualize the effects of the continuum level error and contaminants. DA, as a mean, is the only moment of the flux PDF that does not explicitly depend on spectral resolution or SNR, although both do effect the continuum level placement and line identification. This makes DA easy to use, especially with spectra of low, mixed or poorly known resolution.

The redshift evolution of DA is somewhat slower than given by published analysis of the distribution of individual

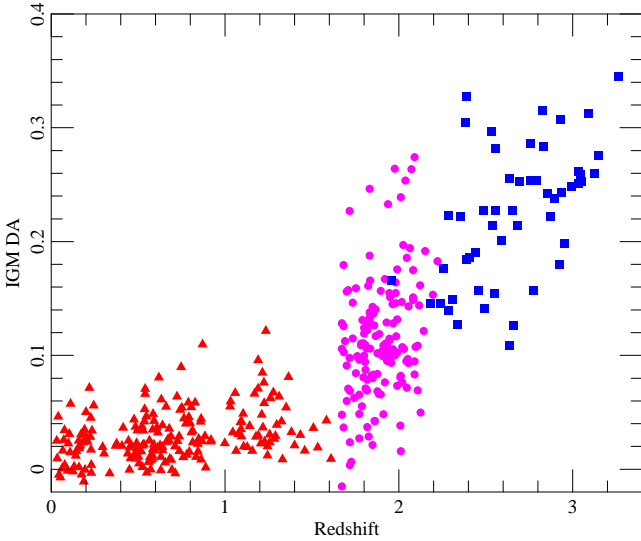


**Figure 8.** The DA as a function of redshift measured in QSO spectra obtained with three spectrographs: FOS (triangles) at the low redshifts, Kast (circles) at intermediate redshifts and HIRES (dark squares) at the highest redshifts. Each point from FOS represents 33.3 Å in the rest frame, as in earlier figures, while the other points are for 121.56 Å in the observed frame from Kirkman et al. (2005). We mask the identified strong Ly $\alpha$  and metals lines in the FOS and HIRES spectra, but we subtract the mean expected amounts of such and metal line absorption from all the Kast points.

**Table 6.** DA as function of redshift from FOS, Kast and HIRES

$z$	DA	$\sigma_{\text{DA}}$
0.20	0.020	0.003
0.40	0.020	0.003
0.60	0.026	0.003
0.80	0.035	0.004
1.00	0.037	0.004
1.20	0.045	0.005
1.40	0.039	0.007
1.60	0.078	0.015
1.80	0.099	0.006
2.00	0.128	0.007
2.20	0.144	0.012
2.40	0.202	0.019
2.60	0.213	0.016
2.80	0.250	0.014
3.00	0.251	0.012
3.20	0.338	0.042

lines. From the DA measured from the flux in pixels, we find  $\gamma + 1 = 1.01$  while Dobrzycki et al. (2002) find  $1 + \gamma \sim 1.5 \pm 0.2$  from fits to the number of lines in all 336 B02 spectra. The difference may be explained by the more rapid evolution of the stronger lines used by Dobrzycki et al. (2002), lines which constitute only 1/3 of the total absorption counted by the flux in the pixels.

The DA for the low density IGM that we measure from the flux in each pixel contains 1.46 times more absorption than is contained in lines seen in the same spectra. This is less than the factor of 3 difference from the larger sample of 336 FOS QSOs, because the large sample is does not have a

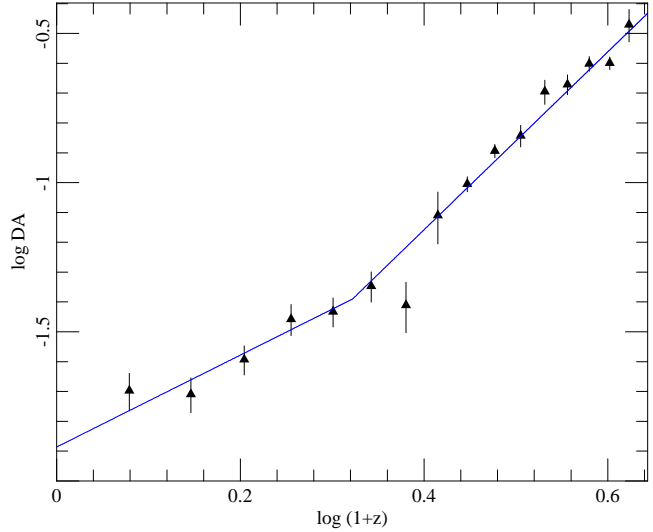


**Figure 9.** log DA as a function of log(1+z) from Table 6. The solid line is the best fit broken power law of Eqn. 6.

uniform minimum rest frame  $W$  value, and it includes spectra with lower SNR – spectra that are less sensitive to weak lines. However, if we fit the distribution of line  $W$  values with an exponential function and we extrapolate this fit to zero  $W$ , we recover most of the missing absorption. The exponential distribution gives approximately the correct amount of absorption that is not in lines seen individually in these FOS spectra. These results are broadly consistent with those from higher redshifts. At  $z = 2.7$  Kirkman & Tytler (1997) found that only half of the absorption came from lines with  $\log N_{\text{HI}} > 14 \text{ cm}^{-2}$  which are the rare saturated lines easily seen in FOS spectra.

The main limitation in line counting is the inability to individually identify lines with low  $W$ . Measurement of DA from flux can include these lines, but they are mostly shallower, and hence more sensitive to the error in the placement of the continuum. The continuum level error is the main error in the DA value, because much of the absorption is from shallow features. This sensitivity to the continuum level is intrinsic to the absorption, and does not depend on how we measure the absorption, from the flux per pixel or from line lists.

We found in Tytler et al. (2004) that we required high SNR spectra to obtain accurate DA values. Here we also need high SNR to give continuum level errors that are not much larger than the DA signal. We limit our measurements to the relatively unusual FOS spectra with  $\text{SNR} > 20$  per pixel.

In addition to the SNR, the continuum error also depends on the the emission lines, the range of wavelengths in a spectrum and the methods used. We fit the continuum by hand because we do not yet have automatic methods that do better. Suzuki et al. (2005) used principal component spectra trained on HST spectra with absorption removed. They then attempted to predict the continuum in the Ly $\alpha$  forest from the components that fit the red side of a spectrum, where the absorption is rare. This was only partly successful, we suspect, because of changes in slope (intrinsic, and from Galactic and atmospheric extinction) across each spectrum.

The emission lines in the Ly $\alpha$  forest are of different

strengths in different QSO spectra. The continuum is harder to fit when the lines are strong (e.g. 0102-2713), especially in low SNR spectra with abundant absorption. We made thin tall plots aligned in rest wavelength to help us find these lines, and make their shapes consistent with the other lines in the spectrum. If we underestimate the strengths of the emission lines, which is readily done, then we will tend to place the continuum too low near those lines, giving systematically too little absorption at their wavelengths. It is very important to see a large portion of each spectrum, well beyond the region of interest for DA, both to establish the general strengths and shapes of the emission lines, and to better distinguish random clumping of photon noise from weak absorption.

The size of the error associated with the DA at a given  $z$  also depends on the rate of change of DA with  $z$ . If DA( $z$ ) were a power law over a wide range of  $z$ , and our measurements were unbiased at all  $z$ , then the error obtained using the power law fit will be very small because we can use points from all  $z$  together. Alternatively, if the true DA( $z$ ) departs from a power law, or if the DA that we measure at some  $z$  is biased, then the error could be systematically larger than we might expect from the plots, tabulated values and errors.

In Tytler et al. (2004) we showed that most of the scatter in the DA at a given  $z \sim 2$  was due to large scale structure. However, some of the scatter in Figs. 2 and 8 could come from variable amounts of systematic error, such as the continuum level too high in one QSO and too low in another, or objects in which we failed to identify and mask metal lines. The scatter in the points at a given  $z$  appears non-Gaussian, with an excess of large deviations. We would not be surprised if some of the outliers had relatively low SNR, leading to unusual continuum level errors, and in the case of the high points, unidentified metal lines.

Overall, the metal lines are probably a smaller source of error in the IGM DA than is the continuum level. Even if the true DA from metal lines were twice our estimates, this would reduce the DA values for the IGM in Table 3 by a factor of 0.85. The STIS spectra also indicate that missing metal lines are not the major error. We obtained similar DA values from FOS and STIS spectra of the same QSOs (Fig. 4), where we conducted an unusually thorough search for metals in the STIS spectra (Milutinović et al. 2006).

In this paper we also measured the flux autocorrelation and the PDF of the flux in the FOS spectra. Both depend on the amount of absorption (DA) as well as the factors that control the distribution of the absorption in wavelength or velocity. These factors include the gas temperature, the Hubble constant, large scale structure and the SNR and spectral resolution. For the FOS spectra the spectral resolution is the dominant factor in the shape of the flux autocorrelation and PDF. However, the FOS sample is large enough that we can measure non-zero autocorrelation out to much larger velocity lags than have been seen in STIS spectra.

The most obvious ways to improve the measurements of the absorption by H I in the IGM would be to include high SNR spectra of tens of QSOs at  $z \simeq 1.6 - 1.8$  with complete wavelength coverage, and to have automated continuum fitting methods that are more accurate than manual methods.

## ACKNOWLEDGMENTS

This work made extensive use of the FOS spectra and line identifications prepared by Jill Bechtold, Jennifer Scott, and Adam Dobrzycki (<http://lithops.as.arizona.edu/~jill/QuasarSpectra/>). This work was supported by HST-AR-10288.01. The NSF REU program supported Samuel Bockenhauer who helped identify metal lines in the STIS spectra.

## REFERENCES

Bahcall J. N., Bergeron J., Boksenberg A., Hartig G. F., Jannuzi B. T., Kirhakos S., Sargent W. L. W., Savage B. D., Schneider D. P., Turnshek D. A., Weymann R. J., Wolfe A. M., 1993, ApJS, 87, 1  
 Bahcall J. N., Bergeron J., Boksenberg A., Hartig G. F., Jannuzi B. T., Kirhakos S., Sargent W. L. W., Savage B. D., Schneider D. P., Turnshek D. A., Weymann R. J., Wolfe A. M., 1996, ApJ, 457, 19  
 Bechtold J., Dobrzycki A., Wilden B., Morita M., Scott J., Dobrzycka D., Tran K., Aldcroft T. L., 2002, ApJS, 140, 143  
 Becker G. D., Rauch M., Sargent W. L. W., 2006, ApJ submitted, astro-ph/0607633  
 Bernardi M., Sheth R. K., SubbaRao M., Richards G. T., Burles S., Connolly A. J., Frieman J., Nichol R., Schaye J., Schneider D. P., Vanden Berk D. E., York D. G., Brinkmann J., Lamb D. Q., 2003, AJ, 125, 32  
 Bi H., 1993, ApJ, 405, 479  
 Bi H., Davidsen A. F., 1997, ApJ, p. 523  
 Davé R., Hernquist L., Katz N., Weinberg D. H., 1999, ApJ, 511, 521  
 Desjacques V., Nusser A., Sheth R. K., 2004, MNRAS in press, astro-ph/0608167  
 Dobrzycki A., Bechtold J., Scott J., Morita M., 2002, ApJ, 571, 654  
 Hernquist L., Katz N., Weinberg D. H., Jordi M., 1996, ApJL, 457, L51  
 Janknecht E., Reimers D., Lopez S., Tytler D., 2006, å, 458, 427  
 Jannuzi B. T., Bahcall J. N., Bergeron J., Boksenberg A., Hartig G. F., Kirhakos S., Sargent W. L. W., Savage B. D., Schneider D. P., Turnshek D. A., Weymann R. J., Wolfe A. M., 1998, ApJS, 118, 1  
 Jena T., Norman M. L., Tytler D., Kirkman D., Suzuki N., Chapman A., Melis C., Paschos P., O'Shea B., So G., Lubin D., Lin W., Reimers D., Janknecht E., Fechner C., 2005, MNRAS, 361, 70  
 Jenkins E. B., Ostriker J. P., 1991, ApJ, 376, 33  
 Kirkman D., Tytler D., 1997, ApJ, 484, 672  
 Kirkman D., Tytler D., Suzuki N., Melis C., Hollywood S., James K., So G., Lubin D., Jena T., Norman M. L., Paschos P., 2005, MNRAS, 360, 1373  
 Kulkarni V. P., Fall S. M., 1993, ApJL, 413, L63  
 McDonald P., Miralda-Escudé J., 2001, ApJL, 549, L11  
 McDonald P., Miralda-Escudé J., Rauch M., Sargent W. L. W., Barlow T. A., Cen R., Ostriker J. P., 2000, ApJ, 543, 1  
 Milutinović N., Lynch R. S., Masiero J. R., Palma C., Misiawa T., Charlton J. C., Kirkman D., Tytler D., 2006, MNRAS in preparation

Oke J. B., Korycansky D. G., 1982, *ApJ*, 255, 11  
 Penton S. V., Shull J. M., Stocke J. T., 2000b, *ApJ*, 544, 150  
 Penton S. V., Stocke J. T., Shull J. M., 2000a, *ApJS*, 130, 121  
 Penton S. V., Stocke J. T., Shull J. M., 2004, *ApJS*, 152, 29  
 Rauch M., 1998, *ARA&A*, 36, 267  
 Rauch M., Miralda-Escude J., Sargent W. L. W., Barlow T. A., Weinberg D. H., Hernquist L., Katz N., Cen R., Ostriker J. P., 1997, *ApJ*, 489, 7  
 Scott J., Bechtold J., Dobrzański A., Kulkarni V. P., 2000, *ApJS*, 130, 67  
 Scott J., Bechtold J., Morita M., Dobrzański A., Kulkarni V. P., 2002, *ApJ*, 571, 665  
 Shull J. M., Penton S. V., Stocke J. T., 1999, *Publications of the Astronomical Society of Australia*, 16, 95  
 Shull J. M., Roberts D., Giroux M. L., Penton S. V., Fardal M. A., 1999, *AJ*, 118, 1450  
 Songaila A., 2004, *AJ*, 127, 2598  
 Suzuki N., Tytler D., Kirkman D., O'Meara J. M., Lubin D., 2005, *ApJ*, 618, 592  
 Tytler D., Kirkman D., O'Meara J., Suzuki N., Orin A., Lubin D., Paschos P., Jena T., Lin W.-C., Norman M., 2004, *ApJ*, 617, 1  
 Tytler D., O'Meara J. M., Suzuki N., Kirkman D., Lubin D., Orin A., 2004, *AJ*, 128, 1058  
 Weymann R. J., Jannuzzi B. T., Lu L., Bahcall J. N., Bergeron J., Boksenberg A., Hartig G. F., Kirhakos S., Sargent W. L. W., Savage B. D., Schneider D. P., Turnshek D. A., Wolfe A. M., 1998, *ApJ*, 506, 1